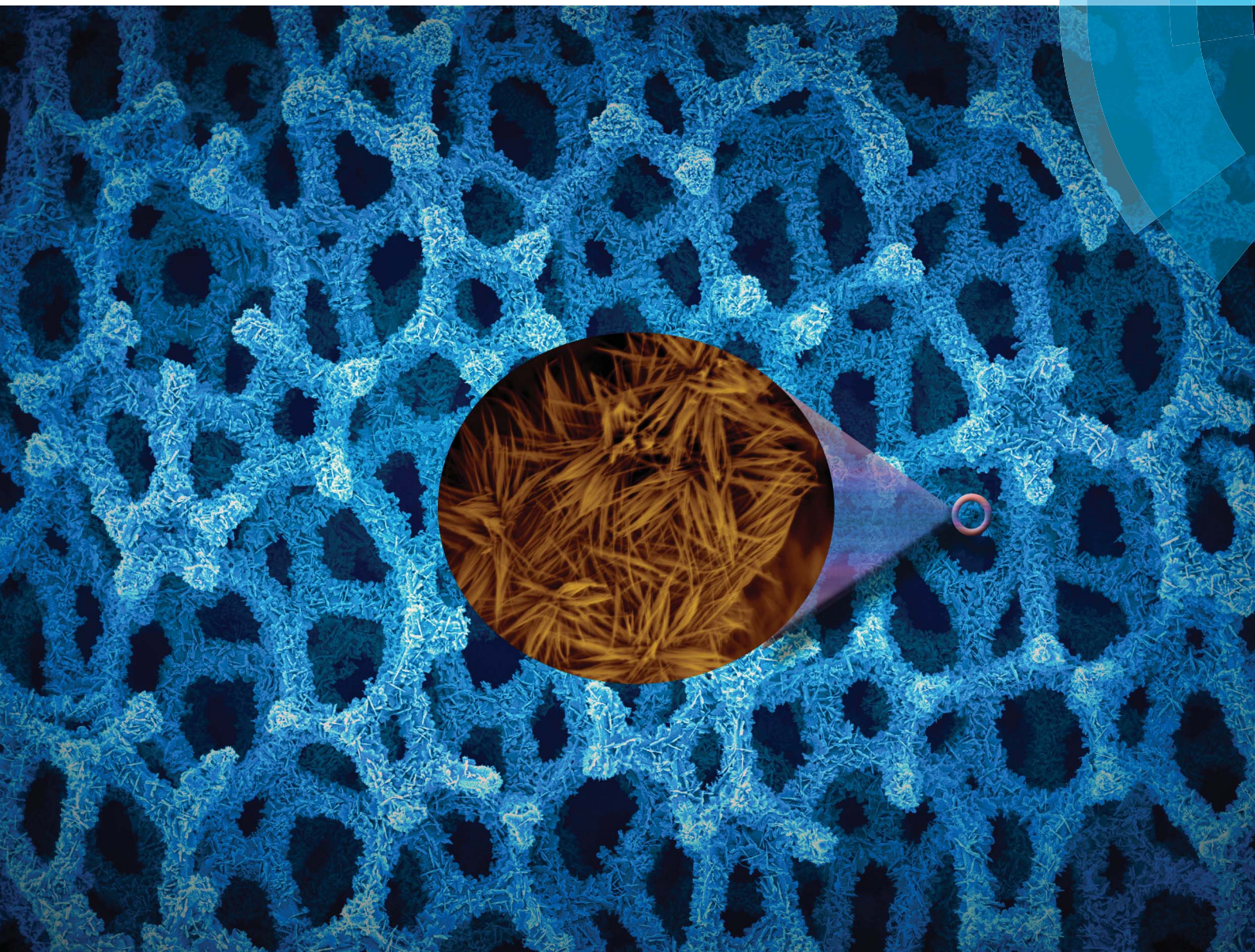


Journal of Materials Chemistry A

Materials for energy and sustainability

www.rsc.org/MaterialsA



ISSN 2050-7488



PAPER

Zirong Tang *et al.*

Synthesis of a nanowire self-assembled hierarchical ZnCo_2O_4 shell/Ni current collector core as binder-free anodes for high-performance Li-ion batteries

Synthesis of a nanowire self-assembled hierarchical ZnCo₂O₄ shell/Ni current collector core as binder-free anodes for high-performance Li-ion batteries†

Cite this: *J. Mater. Chem. A*, 2014, 2, 3741

Hu Long,^a Tielin Shi,^{ab} Shulan Jiang,^b Shuang Xi,^b Rong Chen,^b Shiyuan Liu,^{ab} Guanglan Liao^b and Zirong Tang^{*ab}

In this paper, ZnCo₂O₄ nanowires have been grown and self-assembled as hierarchical structures on a 3D conductive Ni foam substrate. Both leaf-like ZnCo₂O₄ and dandelion-like ZnCo₂O₄ assemblies were synthesized through a hydrothermal process followed by a post-annealing treatment. It is shown that leaf-like assemblies are directly grown on the substrate while dandelion-like assemblies are adsorbed on the surface of the structures. A possible formation mechanism of ZnCo₂O₄ hierarchical structures was proposed. It is shown that these nanowires are porous structures which provide much increased specific surface area. Further work was conducted by taking these Ni foam supported ZnCo₂O₄ structures as binder-free electrodes for Li-ion batteries. Remarkably, the leaf-like ZnCo₂O₄/Ni foam electrode exhibits greatly improved electrochemical performance with high capacity and excellent cycling stability. A high reversible capacity of 1050 mA h g⁻¹ at the rate of 100 mA g⁻¹ was obtained after 60 cycles. Meanwhile, the electrode showed a high rate of 416 mA g⁻¹ with a high capacity of 850 mA h g⁻¹ even after 50 cycles. Our work demonstrates that this unique nanowire self-assembled ZnCo₂O₄ hierarchical structure is promising for high-performance electrochemical energy applications.

Received 4th December 2013
Accepted 3rd January 2014

DOI: 10.1039/c3ta15021f

www.rsc.org/MaterialsA

Introduction

With the fast increasing energy demand in portable electronic devices, electric vehicles and hybrid electric vehicles, extensive attention has been paid to the development of advanced electrode materials for high-performance rechargeable lithium ion batteries (LIBs) which have become the dominant power source for potential green applications.^{1–8} However, as a mainstay of anode material for commercial LIBs, graphite could hardly meet the demand due to the quite low theoretical capacity of only 372 mA h g⁻¹ and relatively poor rate capability.^{5–7} It is essential to develop alternative anode materials with high capacity, long cycling life, and safety.^{5–10}

Recently, transition metal oxides (M_xO_y, M = Sn, Ti, Fe, Mo, Co, *etc.*) have been widely exploited as the anode materials for LIBs exhibiting high reversible capacities (500–1000 mA h g⁻¹).^{2,10–13} Among those transition metal oxides studied so far, Co₃O₄ has been regarded as one of the most promising electrode materials because of its excellent electrochemical

performances such as large capacity and good cyclability.^{14–16} However, due to the toxicity and high cost of cobalt, one of the worthwhile efforts is to partially replace the Co in Co₃O₄ by cheaper and more eco-friendly metals, such as Ni, Zn, Sn and Cu, without sacrificing the electrochemical performance.^{17–22} What is more, these binary metal oxides show an enhanced electrochemical performance because of the improved conductivity and electrochemical activity.^{21,22} As a result, the cobalt-based metal oxide ZnCo₂O₄ which is isostructural to the crystal structure of Co₃O₄ has been realized as a high performance anode material with the replacement of Co²⁺ by Zn²⁺.^{20,23–26} ZnCo₂O₄ is quite attractive because both Zn and Co are electrochemically active with respect to Li.^{19,20,23} Therefore, methods such as the sol-gel method, hydrothermal method and electrospinning method have been developed to fabricate ZnCo₂O₄.^{24–35} It is well-known that the morphology and phase purity of the electrode materials have a crucial effect on electrochemical properties. Different structures of ZnCo₂O₄, such as the nanophase,²⁸ hexagonal shaped nanodisks,²⁹ porous nanotubes,²⁷ microspheres,³⁰ nanorods,³¹ mesoscale three-dimensional (3D) ordered nanocrystals,³⁴ porous nanowires,³⁵ and nanowire arrays/carbon cloth,²⁵ have been successfully fabricated. They exhibit excellent reversible capacity and enhanced cycling performance.

For most demonstrated applications of nanostructured ZnCo₂O₄ in the case of Li-ion batteries, the electrode was fabricated by mixing nanostructured ZnCo₂O₄ with carbon and

^aWuhan National Laboratory for Optoelectronics, Huazhong University of Science and Technology, Wuhan 430074, China

^bState Key Laboratory of Digital Manufacturing Equipment and Technology, Huazhong University of Science and Technology, Wuhan 430074, China. E-mail: zirong@hust.edu.cn

† Electronic supplementary information (ESI) available. See DOI: 10.1039/c3ta15021f

polymer additives/binders and compressing them into pellets.^{27–38} An emerging new concept is to apply additive/binder-free electrodes for LIBs by directly growing electroactive nanostructures on conductive substrates, especially 3D substrates.^{39,40} Direct contact of active nanostructures with conductive substrates can avoid the “dead surface” in traditional slurry-derived electrodes and allows for more efficient charge transfer and mass exchange.⁴⁰

Herein, we report a cost-effective and facile hydrothermal method for the direct growth of ZnCo₂O₄ nanowire self-assembled hierarchical structures on 3D conductive metallic substrate—Ni foam. The unique structure exhibited a large specific surface area, which could effectively increase the electrochemical reaction area and allow better penetration of the electrolyte. Both leaf-like ZnCo₂O₄ and dandelion-like ZnCo₂O₄ structures were obtained. In these unique structures, nanowires in the structures are intercrossed and interconnected with one another, yielding more V-type channels to provide an excellent capability for fast ion and electron transfer. Inspired by these specialities, we investigated their electrochemical performance as electrodes in LIBs, and found that the leaf-like ZnCo₂O₄ structure/Ni foam exhibited excellent performance.

Experimental

Synthesis of ZnCo₂O₄ assemblies/Ni foam

All chemicals were of analytical grade and directly used without further purification. In a typical synthesis procedure, 2 mmol of zinc nitrate (Zn(NO₃)₂·6H₂O) and 4 mmol of cobalt nitrate (Co(NO₃)₂·6H₂O) were dissolved in 70 ml of deionized water at room temperature to form a clear pink solution, followed by addition of 4 mmol of ammonium fluoride (NH₄F) and 10 mmol of urea (CO(NH₂)₂) and the mixture was dispersed to form a homogeneous solution by constant intense stirring. The Ni foam was immersed in a 3 M hydrochloric acid (HCl) solution for 10 min to get rid of the possible surface oxide layer before it was put into the bottle for reaction. After two pieces of cleaned Ni foams were dropped into the solution, it was then transferred into a Teflon-lined stainless autoclave. The autoclave was sealed and heated to 120 °C in an electric oven. After reaction for 12 h, the autoclave cooled down to room temperature naturally and the samples were taken out. One piece of sample was processed with ultrasonication in ethanol for 20 min while the other one was rinsed with ethanol and distilled water for several times. Then the samples were dried at 60 °C in an oven overnight. In the next step, the samples were put in a quartz tube and were calcined at 400 °C for 2 h with a ramping rate of 2 °C min⁻¹, then the samples were used for a later study.

Materials characterization

The morphology of the products was characterized using field-emission scanning electron microscopy (FESEM, JEOL JSM-6700F) with an energy dispersive X-ray (EDX) attachment, transmission electron microscopy (TEM, FEI, Tecnai G2 20) and field-emission transmission electron microscopy (FETEM, FEI, Tecnai G2 F30). Crystal structures of products were

characterized with an X-ray diffractometer (XRD; X'Pert PRO, PANalytical B.V., The Netherlands) with radiation from a Cu target (K α , λ = 0.15406 nm). X-ray photoelectron spectroscopy (XPS) measurements were carried out on a VG MultiLab 2000 system with a monochromatic Al K X-ray source (Thermo VG Scientific). Specific surface areas were computed from the results of N₂ physisorption at 77 K (Micromeritics ASAP 2020) by using the Brunauer–Emmett–Teller (BET) and Barrett–Joyner–Halenda (BJH) methods.

Electrochemical measurements

The sample was cut into many smaller round pieces with a diameter of 12 mm. Both the ZnCo₂O₄ coated Ni foam and bar Ni foam were weighed in a high-precision analytical balance (Sartorius, max weight 210 mg, d = 0.01 mg). The reading difference was the exact mass for the coated samples on Ni foam. The loading density of ZnCo₂O₄ in the sample processed with ultrasonication was calculated to be around 1.06–1.92 mg cm⁻². The loading density of ZnCo₂O₄ in the sample without ultrasonication was calculated to be around 4.42–6.85 mg cm⁻².

The electrochemical performance of the as-synthesized ZnCo₂O₄ product was investigated by using it as a binder-free anode in LIBs in coin-type half-cells, which were laboratory-assembled by a CR2032 press in an argon-filled glove box with oxygen and water contents below 1 and 0.1 ppm, respectively. A pure lithium foil was used as the counter electrode as well as the reference electrode. A piece of ZnCo₂O₄/Ni foam was used directly as the working electrode and Celgard 2400 polymer separators were employed. The electrolyte was 1 M LiPF₆ in ethylene carbonate (EC) and diethyl carbonate (DEC) (1 : 1 by volume). The cells were then aged for 12 h before the measurements to ensure full percolation of the electrolyte to the electrodes. Coin-type half-cells were cycled at various current densities and a voltage range of 0.01–3 V (vs. Li⁺/Li) at room temperature with a multichannel battery measurement system (Land, China). Cyclic voltammetry (CV) and electrochemical impedance spectra (EIS) experiments were conducted on an Autolab work station (PGSTAT-302N, Eco Chemie B.V. Company). The CV experiment was carried out in the range of 0.01–3.0 V (vs. Li⁺/Li) and at a scan rate of 0.1 mV s⁻¹. The EIS experiment was carried out at a frequency range of 0.01 Hz–100 kHz at an amplitude of 10 mV versus the open circuit potential.

Results and discussion

Structural and morphological characterization

The composition and phase purity of the as prepared ZnCo₂O₄ structures were examined by peeling off the Ni foam and then using X-ray diffraction. As shown in Fig. 1, all the diffraction peaks of ZnCo₂O₄ structures in black line are consistent with the values in the standard card of cubic ZnCo₂O₄ with a spinel structure (JCPDS card no. 23-1390). No additional diffraction peaks other than ZnCo₂O₄ were detectable, implying the high purity of the product.

The morphology structure of the as-synthesized ZnCo₂O₄/Ni foam is shown in Fig. 2. Fig. 2a–d show the typical morphology

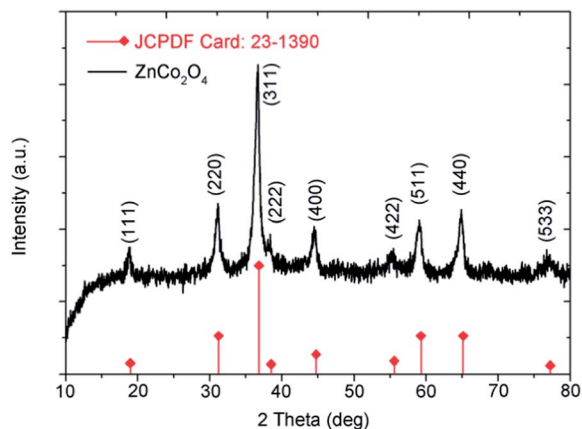


Fig. 1 XRD pattern of the as prepared ZnCo_2O_4 structures peeled off from the Ni foam.

of the as-synthesized ZnCo_2O_4 structures on Ni foam without ultrasonication, while Fig. 2e–h show the ZnCo_2O_4 structures on Ni foam after ultrasonication for 20 min. From the low magnification SEM image in Fig. 2a and e, the structure can be described as a Ni foam core with a uniformly coated shell of hierarchical ZnCo_2O_4 nanoassemblies. The optical images of the Ni foam, the as-prepared precursor coated Ni foam in pink, and Ni foam after ZnCo_2O_4 growth in black are shown in Fig. S1.† The obvious color change of the three samples indicates the uniform coating of ZnCo_2O_4 . From the enlarged views in Fig. 2b, it can be observed that the Ni foam was uniformly coated with ball-like structures. Higher-magnification SEM images shown in Fig. 2c and d provide clearer information about the ZnCo_2O_4 structure, revealing that the sample surface without ultrasonication was actually covered by dandelion-like ZnCo_2O_4 assemblies. For convenience, dandelion-like ZnCo_2O_4 is termed as DZCO in the following discussion. The diameter of the DZCO structure was about $18\ \mu\text{m}$, and the nanowires in the dandelion were radially grown around the center. Meanwhile, the ZnCo_2O_4 nanostructures directly precipitated from the same

growth solution and had exactly the same dandelion-like morphology as that which appeared on Ni foam.

On the other hand, the sample after ultrasonication for 20 min shows a different surface morphology, although the structure also looks like the Ni foam core covered with the shell of nanoassemblies. Fig. 2e to g show the sample with magnification from low to high. From Fig. 2g, it can be inferred that the flake-like structures vertically grown on the substrate are actually nanowires in self-assembled clusters. The nanowires in the clusters were radially grown around one point just like a small leaf. As shown in Fig. 2h, we can see that the radially grown nanowires have uniform diameters of 80–100 nm and lengths of about $5\ \mu\text{m}$. Such a nanowire self-assembled leaf-like ZnCo_2O_4 structure provides a high surface area that is beneficial to an electrode material. For convenience, leaf-like ZnCo_2O_4 is termed as LZCO in the following discussion.

Further information about the product is provided by transmission electron microscopy (TEM) in Fig. 3. The crystal structure of spinel ZnCo_2O_4 is illustrated in Fig. 3a. Fig. 3b shows the low-magnification TEM image of two neighboring LZCO clusters, where radially grown nanowires can be seen, revealing that the average size of the nanowire is the same as that from the SEM observation. The higher magnification TEM image of the nanowires shown in Fig. 3c reveals that typical ZnCo_2O_4 nanowires assembling the leaf structures exhibit a conical shape and the surface of the nanowires is rough, suggesting that the nanowire composed of many nanoparticles instead of a single-crystalline nanowire is actually a porous structure. The porous structures were formed mainly because of the release of CO_2 gas during the crystallization under the annealing process. Fig. 3d shows the HRTEM image of an individual ZnCo_2O_4 nanowire. It indicates that there are two types of lattice fringes with lattice spacings of 0.246 and 0.463 nm, which were in good agreement with the (311) and (111) plane of ZnCo_2O_4 . As shown in Fig. S2†, the relevant SAED pattern shows distinct diffraction rings which could be assigned to ZnCo_2O_4 .

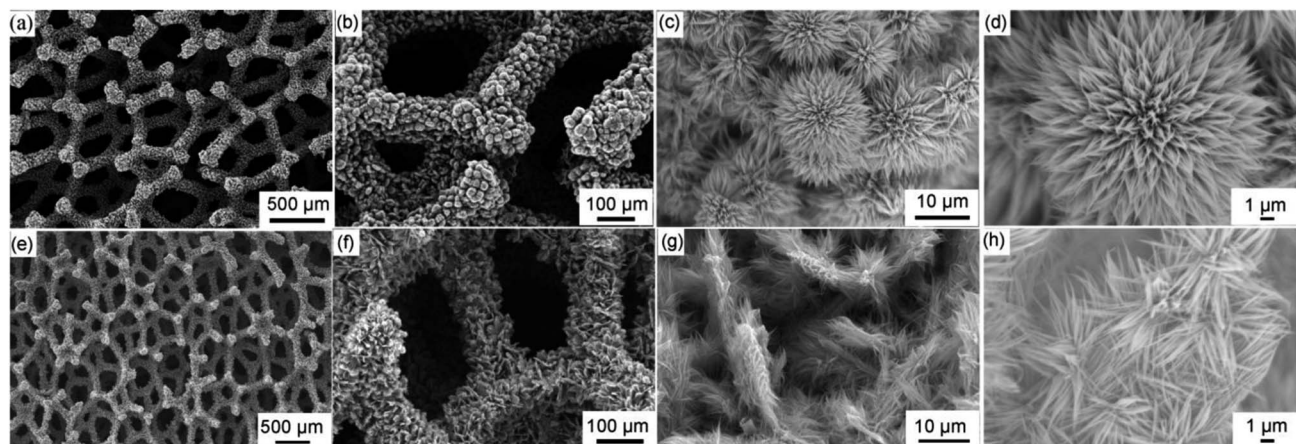


Fig. 2 (a–d) Typical SEM images of the DZCO structure coated Ni foam without ultrasonication; (e–h) SEM image of the LZCO structure on Ni foam obtained after ultrasonication for 20 min.

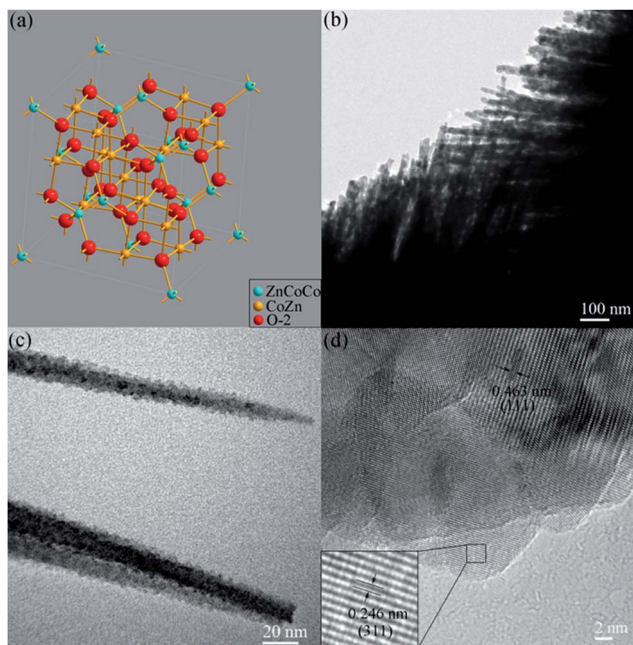


Fig. 3 (a) The crystal structure of spinel ZnCo_2O_4 . (b) Low-magnification TEM image of two neighboring LZCO clusters. (c) Low-magnification TEM image of the ZnCo_2O_4 nanowires. (d) HRTEM image of the ZnCo_2O_4 nanowire.

Important information about the surface electronic state and the composition of the porous ZnCo_2O_4 leaf was analysed by XPS. Fig. 4a shows a typical full wide-scan XPS spectrum of the products, where the existing characteristic peaks confirm the presence of Zn, Co, O, and C elements. No other peaks are observed. The binding energy in XPS analysis for C 1s peak at 284.6 eV was used as the reference for calibration. Fig. 4b shows the high-resolution Zn 2p spectrum. Two peaks located at 1020.3 and 1043.6 eV are assigned to Zn 2p_{3/2} and Zn 2p_{1/2}, respectively, indicating the Zn(II) oxidation state of ZnCo_2O_4 .

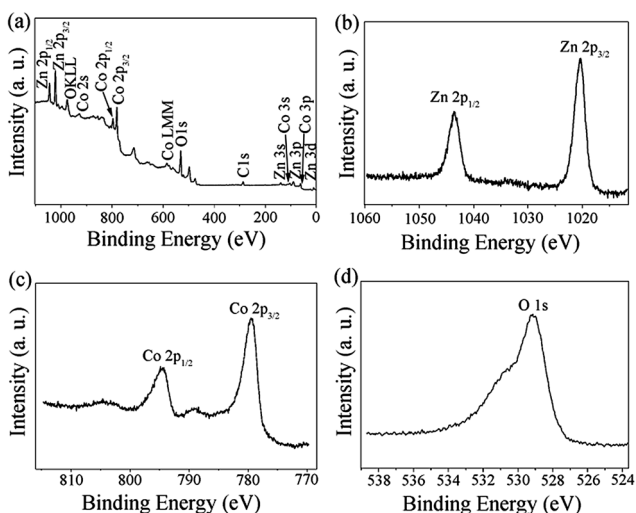


Fig. 4 XPS spectra for the ZnCo_2O_4 structure: (a) survey spectrum and high-resolution (b) Zn 2p, (c) Co 2p and (d) O 1s spectra.

Fig. 4c shows the high-resolution Co 2p spectrum. Two peaks at 779.4 eV for Co 2p_{3/2} and 794.8 eV for Co 2p_{1/2} are observed, confirming the Co(III) oxidation state of ZnCo_2O_4 . As shown in Fig. 4d, the O 1s peak corresponds to the oxygen species in ZnCo_2O_4 . From the above analysis, the XPS results in conjunction with XRD data confirm the formation of ZnCo_2O_4 with a normal spinel structure.

The specific surface area and pore size distribution in the hierarchical nanostructures were determined by BET N_2 adsorption-desorption analysis at 77 K, as shown in Fig. 5. The prepared sample exhibits a specific surface area of $154.7951 \text{ m}^2 \text{ g}^{-1}$ and a pore volume of $0.42 \text{ cm}^3 \text{ g}^{-1}$. Compared with the reported values of surface area of ZnCo_2O_4 (BET(nanowires) = $68.86 \text{ m}^2 \text{ g}^{-1}$, BET(microspheres) = $26.8 \text{ m}^2 \text{ g}^{-1}$, BET(nanotubes) = $21.9 \text{ m}^2 \text{ g}^{-1}$, BET(hollow microspheres) = $20.9 \text{ m}^2 \text{ g}^{-1}$ and BET(nanoparticles) = $11.5 \text{ m}^2 \text{ g}^{-1}$), this is the largest specific surface area in a ZnCo_2O_4 material until now.^{26,27,30,33,36} The large specific surface area could effectively increase the electrochemical reaction area and allow better penetration of the electrolyte.³⁹

The pore size distribution, derived from desorption data and calculated from the isotherm using the BJH model (the inset of Fig. 5), shows that most of the pores fall into the size range of 2 to 10 nm. The porous ZnCo_2O_4 structure can buffer the large volume change of anodes during the repeated Li^+ insertion-extraction.³⁹

Growth analysis and formation mechanism

Comparing the products before and after ultrasonication shown in Fig. 2, we can find that the dandelion-like structures disappeared after ultrasonication for 20 min, while the leaf-like structure remained and still adhered robustly to the substrate maintaining its integrated architecture. In fact, the dandelion-like and leaf-like structures are nanowire self-assembled clusters. Considering this, a possible formation mechanism of the hierarchical ZnCo_2O_4 structure is proposed and schematically illustrated in Fig. 6.

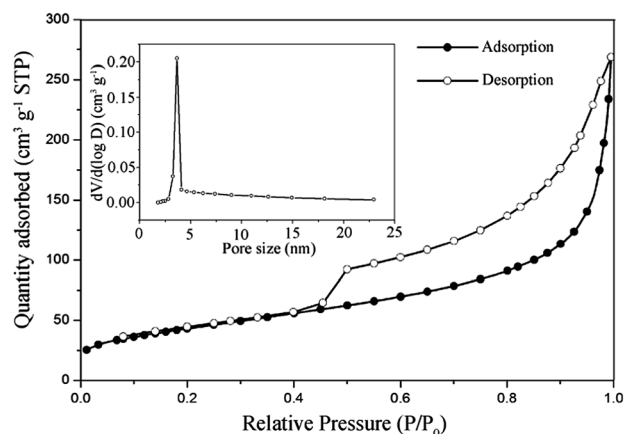


Fig. 5 Nitrogen adsorption and desorption isotherms of the ZnCo_2O_4 structure. Inset: corresponding pore distribution derived from desorption data and calculated from the isotherm using the BJH model.

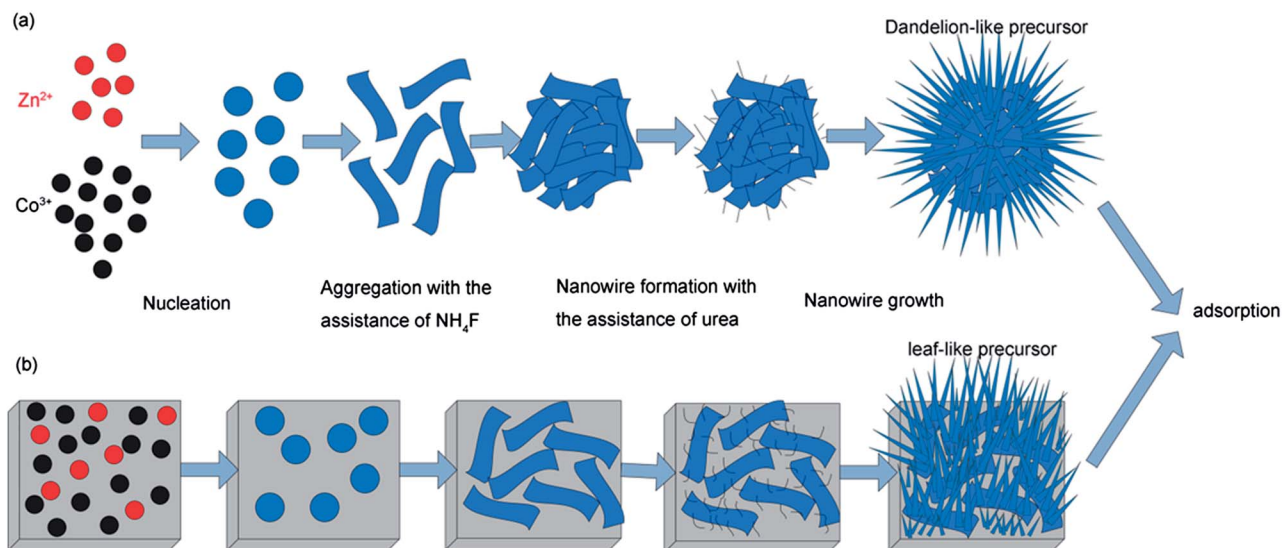


Fig. 6 Schematic illustration of the morphology evolution of the ZnCo_2O_4 structure: (a) scheme of dandelion-like precursor evolution in reaction solution; (b) scheme of leaf-like precursor evolution on the substrate.

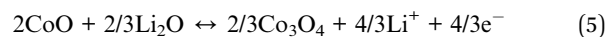
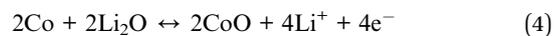
At the initial stage of the synthesis process, the Zn^{2+} and Co^{3+} ions began to nucleate and form nanoparticles that possessed high surface energies. During this stage, the newly produced nanoparticles tended to aggregate into nanosheets with the help of NH_4F .⁴⁰ NH_4F largely enhanced the adhesion between the substrate and the nanosheet.⁴⁰ These nanosheets in solution finally aggregated into microspheres driven by minimization of the surface energy of the system, while the nanosheets on the substrate retained their morphology.^{26,40} Then, nanowires grew on the surface of the nanosheets or microspheres due to the urea that was added as a surfactant for the growth of the nanowires on the plates.^{26,40} Afterwards, the structure continued to grow into leaf-like precursors on the substrate and dandelion-like precursors in the solution respectively. Finally some dandelion-like precursors were adsorbed onto the leaf-like precursors grown on Ni foam, forming the final structures shown in Fig. 2a–d. It can be concluded that both leaf-like and dandelion-like ZnCo_2O_4 are formed with the help of NH_4F and urea. The only difference is that the nanosheets on the substrate cannot aggregate into microspheres because of the adhesion force with the substrate, while the nanosheets in the solution aggregated to microspheres, leading to the formation of different nanostructures. Such a mechanism is commonly used to explain the crystal growth process and was observed for similar material systems, such as, Co_3O_4 , NiCo_2O_4 (shown in ESI Fig. S3†) and so on.^{26,40,41} Several factors, such as Ostwald ripening, crystal-face attraction, van der Waals forces and hydrogen bonds, were considered to contribute to the self-assembly.²⁶

Electrochemical characteristics

For convenience, the sample without ultrasonication is denoted as DZCO/LZCO/Ni and the sample after ultrasonication is named LZCO/Ni in the following discussion.

Both samples were configured as laboratory-based CR2032 coin cells to investigate the electrochemical performance without using ancillary binders or conducting additives. Besides, as it was reported for Ni foam substrate based anodes in the literature (ref. 38, 41–44), the cleaned Ni foam offers negligible contribution to the electrochemical performance of the configuration. Galvanostatic charge–discharge tests were performed to investigate the lithium insertion/extraction behaviour of the as-prepared ZnCo_2O_4 based electrodes at a voltage window of 0.01–3 V vs. Li^+/Li , and the electrochemical performance is presented in Fig. 7.

According to previous studies, the electrochemical reactions of ZnCo_2O_4 involved in the lithium insertion and extraction reactions can be illustrated as follows:^{25–35}



Typical cyclic voltammograms (CVs) of the LZCO/Ni electrode are displayed in Fig. S4.† The first discharge cycle exhibits a sharp reduction peak at 0.63 V in the cathodic process, which can be assigned to the reduction of ZnCo_2O_4 to Zn and Co as shown in eqn (1).^{27,29} In the anodic polarization process, two broad peaks were observed at 1.60 and 2.1 V, which can be attributed to the oxidation of Zn to Zn^{2+} and Co to Co^{3+} .²⁹ Different from the first cycle, the second and third cycles show that the reduction peak is gradually moved to about 0.9 V and becomes much broader, indicative of different electrochemical reactions governing the two processes.^{29,35} Similar shifts in

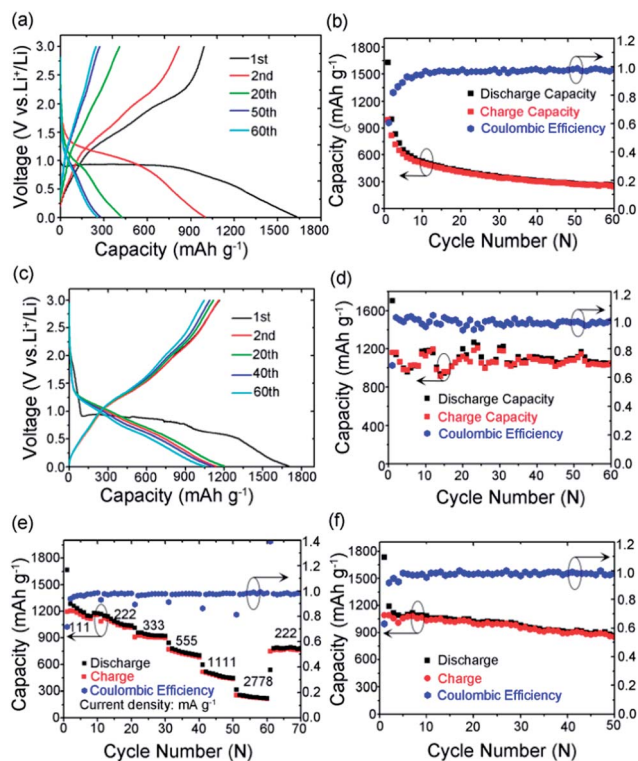


Fig. 7 (a and c) Representative galvanostatic discharge–charge voltage profiles at a current density of 100 mA g^{-1} in the voltage range of 0.01–3 V: (a) DZCO/LZCO/Ni electrode; (c) LZCO/Ni electrode; (b and d) charge and discharge capacity versus cycle number at 100 mA g^{-1} and the corresponding Coulombic efficiencies: (b) DZCO/LZCO/Ni electrode; (d) LZCO/Ni electrode. (e) The rate performance of the LZCO/Ni electrode at various current densities. (f) Capacity of the LZCO/Ni electrode versus cycle number at current densities of 416 mA g^{-1} and the corresponding Coulombic efficiency.

voltage values of the anodic/cathodic peaks were reported in the CV curves of ZnCo_2O_4 nanostructures.^{27,29,30,35} Compared with other ZnCo_2O_4 nanostructures, the slight differences in the peak values are attributed to the different preparation methods.

Fig. 7a and c show the representative voltage–capacity profiles of DZCO/LZCO/Ni and LZCO/Ni electrodes during discharge (Li^+ insertion) and charge (Li^+ extraction) processes in a voltage window of 0.01–3 V at a current rate of 100 mA g^{-1} . From those curves, it can be seen that all discharge curves exhibit a distinct plateau between 0.8 and 1.2 V. There is a wide, steady discharging plateau at 1 V in the first discharge process, followed by a long slope between 1.0 and 0.50 V. In the following cycles, the long discharging plateau becomes steeper and moves upward, and is slightly higher than that of the first discharge curve, which is similar to the previous reports.^{28,36} The discharge plateau at about 1 V disappeared in the next voltage profile indicating the formation of a stable solid electrolyte interphase (SEI) in the first cycle.

As shown in Fig. 7a and b, the initial discharge and charge capacities of the DZCO/LZCO/Ni electrode are 1633 and $990.9 \text{ mA h g}^{-1}$, respectively. The first cycle irreversible capacity loss of 39.3% could be due to the SEI formation and the reduction of metal oxide to metal with Li_2O formation.^{46–49} The ultrahigh

initial discharge capacity may be due to the larger surface area compared with other morphologies of the ZnCo_2O_4 material.

Fig. 7b shows the charge and discharge capacity of the DZCO/LZCO/Ni electrode versus cycle number at 100 mA g^{-1} and the corresponding Coulombic efficiencies. It can be seen that the DZCO/LZCO/Ni electrode reveals a large capacity fading during the 50th cycle. The DZCO/LZCO/Ni anode retained a capacity of 255 mA h g^{-1} after 60 cycles. As schematically illustrated in Fig. 6, the DZCO assemblies were actually adsorbed on the LZCO assemblies with an unstable connection. Upon lithiation, the nanostructured ZnCo_2O_4 will expand with anisotropic change. Associated with such a volume expansion, the anode materials are subject to detachment, leading to the loss of electrical contact and rapid capacity fading of the battery.

For comparison, Fig. 7c and d show the voltage–capacity profiles, capacity retention of the LZCO/Ni electrode at 100 mA g^{-1} . The initial discharge and charge capacities of LZCO/Ni are 1703.9 and 1166 mA h g^{-1} , respectively, revealing a first cycle irreversible capacity loss of 31.6%, better than that of the DZCO/LZCO/Ni electrode. As can be seen in Fig. 7c, the good superposition of the charge and discharge voltage–capacity profiles after the first cycle indicates good electrochemical reversibility and stability in the lithium insertion and extraction reactions.

The charge, discharge capacity and corresponding Coulombic efficiencies of the LZCO/Ni electrode versus cycle number are shown in Fig. 7d. The electrode reveals a capacity fluctuation during cycles but still maintains a nearly constant value above 1150 mA h g^{-1} which is in accordance with the results of discharge–charge profiles in Fig. 7b. The turbulence of capacity in the first 35 cycles may result from the decomposition of the metal oxides. On the one hand, decomposition of the metal oxides leads to a decrease of capacity. On the other hand, the decomposition of the metal oxides may lead to the formation of a polymeric surface layer and metal nanoparticles on the active material which builds-up on the surface and within the pores of the porous active material, and thus increases the storage.^{26,27} Even after 60 cycles, a high discharge capacity of 1100 mA h g^{-1} is still retained, demonstrating the high specific capacity and superior cyclability, which is consistent with the voltage–capacity profiles. The specific capacity is higher than the theoretical value (903 mA h g^{-1} , 8.33 mol Li) reported in the literature. This extra capacity phenomenon is common in almost all transition metal oxide anodes, which has been ascribed to the reversible growth of polymeric gel-like films on the surface of active materials.^{25–29,50–53}

The superior capacity and cyclability of the LZCO/Ni foam can be mainly ascribed to the hierarchical 3D porous structure and a direct growth on the conductive substrate. Considering that no ancillary materials such as polymer binders and carbon black are used in the present work, the present LZCO/Ni is a suitable candidate for electrodes of high performance LIBs.

To further demonstrate the excellent performance of the LZCO/Ni electrodes, their electrochemical properties were studied by charging/discharging at different current densities ranging from 111 to 2778 mA g^{-1} and the results are displayed in Fig. 7e, and their representative charge–discharge voltage profiles are shown in Fig. S5.† As the current density gradually

increases from 111, 222, 333, 555, 1111 to 2778 mA g⁻¹, the average discharge capacity decreases from 1180, 1100, 940, 730, 485 to 240 mA h g⁻¹, respectively. When the current density was tripled from 111 to 333 mA g⁻¹, the capacity reduced from 1180 to 940 mA h g⁻¹. Even when the current density was as high as 1111 mA g⁻¹, a capacity of around 485 mA h g⁻¹ was still available, which is higher than the theoretical capacity of the graphite anode of 372 mA h g⁻¹. More importantly, after the high rate discharge-charge cycles, a discharge capacity of 790 mA h g⁻¹ could be resumed and maintained for another 10 cycles without obvious decay when the current density was 222 mA g⁻¹ again.

We further investigated the cycling behaviour of the LZCO/Ni electrode at a relatively high current density of 416 mA g⁻¹ for 50 cycles as shown in Fig. 7f. The corresponding charge-discharge voltage profiles are shown in Fig. S6.† It is found that there is only a slight drop in the discharge capacity during the initial discharge-charge cycle, showing excellent cycling stability of the electrode. The specific capacity still remains at 900 mA h g⁻¹ even after 48 cycles, which is close to the theoretical capacity of 903 mA h g⁻¹. In addition, the coulombic efficiency between the discharge and charge capacities of the samples at 416 mA h g⁻¹ is higher than 97%, indicating excellent electrochemical reversibility during the lithium insertion and extraction reactions.

The Nyquist plot of the LZCO/Ni electrode after the first cycle is shown in Fig. S7.† Based on the equivalent electrical circuit model shown in the inset of Fig. S7†, the solution resistance (R_s) and the calculated charge transfer resistance (R_{ct}) of the cells are 8.1 Ω and 95.4 Ω, respectively. The surface layer resistance is obviously small, which can benefit the diffusion of the Li ions.^{30,31}

These test results of LIBs reveal a high specific capacity, excellent cycling stability, and outstanding rate performance, which can be mainly ascribed to the hierarchical 3D porous structure with a high specific surface area and the direct growth of active materials on a conductive substrate. Firstly, the larger surface area compared to previously reported ZnCo₂O₄ material can not only accommodate the stress induced by the volume change during the electrochemical reaction, but also lead to a higher efficiency of the lithiation and delithiation process. Secondly, the unique 3D structure of the electrode with more “V-type” channels has an increased portion of the exposed surface which provides more active sites for access to Li⁺ ions.^{41,46,54-57} This speciality facilitates ion/electron transport inside active materials, diffusion of the electrolyte, and enough contact area between the electrolyte and the active electrodes in a short time for fast energy storage according to previous reports.^{1,40,54-56} Moreover, the porosity on the surface which was demonstrated by TEM and BET results further shortens the diffusion paths of lithium ions and enhances the rate capability. Meanwhile, LZCO assemblies are found to have a direct growth on conductive Ni foam and their excellent adhesion provides a better electrical contact between ZnCo₂O₄ and the substrate, which also shortens the charge transfer pathway and lowers the exchange resistance for Li ions between active materials and the electrolyte.^{1,45,56-59} All the above characteristics will undoubtedly

lead to enhanced electrochemical performance for high performance LIBs.

Conclusions

In summary, ZnCo₂O₄ nanowire self-assembled hierarchical structures have been grown on 3D conductive Ni foam substrates through a simple solution method together with a post-annealing treatment. Both dandelion-like ZnCo₂O₄ and leaf-like ZnCo₂O₄ assemblies were observed. The hierarchical structures exhibited larger specific surface area compared with the literature reported ZnCo₂O₄ material.

These Ni foam supported ZnCo₂O₄ structures were directly used as binder-free electrodes for LIBs. It is shown that the leaf-like ZnCo₂O₄/Ni foam electrode exhibits very high electrochemical capacity and excellent cycling stability. The leaf-like ZnCo₂O₄/Ni foam electrode presents a high reversible capacity of 1050 mA h g⁻¹ at a rate of 100 mA g⁻¹ after 60 cycles, and shows a high rate of 416 mA g⁻¹ with a high capacity of 850 mA h g⁻¹ even after 50 cycles. Such binder-free electrodes obtained by directly growing one-dimensional nanostructures of electroactive materials on conductive substrates are promising for the fabrication of high performance energy storage devices.

Acknowledgements

We acknowledge the financial support of the National Natural Science Foundation of China (no. 51275195 and 91323106) and the Hubei Provincial Natural Science Foundation of China (no. 2012FFB02216).

Notes and references

- 1 K. T. Nam, D. W. Kim, P. J. Yoo, C. Y. Chiang, N. Meethong, P. T. Hammond, Y. M. Chiang and A. M. Belcher, *Science*, 2006, **312**, 885–888.
- 2 P. Poizot, S. Laruelle, S. Grugeon, L. Dupont and J. M. Tarascon, *Nature*, 2000, **407**, 496–499.
- 3 J. M. Tarascon and M. Armand, *Nature*, 2001, **414**, 359–367.
- 4 A. S. Arico, P. Bruce, B. Scrosati, J. M. Tarascon and W. V. Schalkwijk, *Nat. Mater.*, 2005, **4**, 366–377.
- 5 K. S. Kang, Y. S. Meng, J. Breger, C. P. Grey and G. Ceder, *Science*, 2006, **311**, 977.
- 6 B. Scrosati, *Nat. Nanotechnol.*, 2007, **2**, 598–599.
- 7 M. Armand and J. M. Tarascon, *Nature*, 2008, **451**, 652.
- 8 B. Kang and G. Ceder, *Nature*, 2009, **458**, 190.
- 9 J. Cabana, L. Monconduit, D. Larcher and M. R. Palacin, *Adv. Mater.*, 2010, **22**, 170–192.
- 10 S. Hossain, Y. K. Kim, Y. Saleh and R. Loutfy, *J. Power Sources*, 2003, **114**, 264–276.
- 11 D. V. Bavykin, J. M. Friedrich and F. C. Walsh, *Adv. Mater.*, 2006, **18**, 2807–2824.
- 12 L. Taberna, S. Mitra, P. Poizot, P. Simon and J. M. Tarascon, *Nat. Mater.*, 2006, **5**, 567–573.
- 13 N. Kang, J. H. Park, J. Choi, J. Jin, J. Chun, I. G. Jung, J. Jeong, J. G. Park, S. M. Lee, H. J. Kim and S. U. Son, *Angew. Chem., Int. Ed.*, 2012, **51**, 6626.

- 14 Y. Liu and X. Zhang, *Solid State Ionics*, 2013, **231**, 63–68.
- 15 P. Meduri, E. Clark, J. H. Kim, E. Dayalan, G. U. Sumanasekera and M. K. Sunkara, *Nano Lett.*, 2012, **12**, 1784.
- 16 S. L. Xiong, J. S. Chen, X. W. Lou and H. C. Zeng, *Adv. Funct. Mater.*, 2012, **22**, 861.
- 17 Y. M. Kang, K. T. Kim, J. H. Kim, H. S. Kim, P. S. Lee, J. Y. Lee, H. K. Liu and S. X. Dou, *J. Power Sources*, 2004, **133**, 252.
- 18 Y. Q. Chu, Z. W. Fu and Q. Z. Qin, *Electrochim. Acta*, 2004, **49**, 4815.
- 19 Y. Sharma, N. Sharma, G. V. Subba Rao and B. V. R. Chowdari, *Chem. Mater.*, 2008, **20**, 6829–6839.
- 20 R. Alcantara, M. Jaraba, P. Lavela and J. L. Tirado, *Chem. Mater.*, 2002, **14**, 2847.
- 21 Z. Wang, Z. Wang, W. Liu, W. Xiao and X. W. Lou, *Energy Environ. Sci.*, 2013, **6**, 87.
- 22 Z. Wang, Z. Wang, H. Wu and X. W. Lou, *Sci. Rep.*, 2013, **3**, 1391.
- 23 C. Ai, M. Yin, C. Wang and J. Sun, *J. Mater. Sci.*, 2004, **39**, 1077.
- 24 X. Wei, D. Chen and W. Tang, *Mater. Chem. Phys.*, 2007, **103**, 54–58.
- 25 B. Liu, J. Zhang, X. Wang, G. Chen, D. Chen, C. Zhou and G. Shen, *Nano Lett.*, 2012, **12**, 3005.
- 26 L. Hu, B. Qu, C. Li, Y. Chen, L. Mei, D. Lei, L. B. Chen, Q. Li and T. Wang, *J. Mater. Chem. A*, 2013, **1**, 5596–5602.
- 27 W. Luo, X. Hu, Y. Sun and Y. Huang, *J. Mater. Chem.*, 2012, **22**, 8916–8921.
- 28 Y. Sharma, N. Sharma, G. V. S. Rao and B. V. R. Chowdari, *Adv. Funct. Mater.*, 2007, **17**, 2855–2861.
- 29 Y. Qiu, S. Yang, H. Deng, L. Jin and W. Li, *J. Mater. Chem.*, 2010, **20**, 4439–4444.
- 30 Q. Xie, F. Li, H. Guo, L. Wang, Y. Chen, G. Yue and D. Peng, *ACS Appl. Mater. Interfaces*, 2013, **5**, 5508–5517.
- 31 Z. Jia, D. Ren, Q. Wang and R. Zhu, *Appl. Surf. Sci.*, 2013, **270**, 312–318.
- 32 C. W. Lee, S. D. Seo, D. W. Kim, S. Park, K. Jin, D. W. Kim and K. S. Hong, *Nano Res.*, 2013, **6**, 348–355.
- 33 M. V. Reddy, K. Y. H. Kenrick, T. Y. Wei, G. Y. Chong, G. H. Leong and B. V. R. Chowdari, *J. Electrochem. Soc.*, 2011, **158**, 1423–1430.
- 34 D. Deng and J. Y. Lee, *Nanotechnology*, 2011, **22**, 355401.
- 35 H. Liu and J. Wang, *Electrochim. Acta*, 2013, **92**, 371–375.
- 36 N. Du, Y. Xu, H. Zhang, J. Yu, C. Zhai and D. Yang, *Inorg. Chem.*, 2011, **50**, 3320–3324.
- 37 B. Hymavathi, B. R. Kumar and T. S. Rao, *AIP Conf. Proc.*, 2012, **1461**, 299–302.
- 38 C. Ai, M. Yin, C. Wang and J. Sun, *J. Mater. Sci.*, 2004, **39**, 1077–1079.
- 39 C. Kim, M. Noh, M. Choi, J. Cho and B. Park, *Chem. Mater.*, 2005, **17**, 3297.
- 40 Y. Chen, B. Qu, L. Hu, Z. Xu, Q. Li and T. Wang, *Nanoscale*, 2013, **5**, 9812.
- 41 J. P. Liu, C. W. Cheng, W. W. Zhou, H. X. Li and J. F. Hong, *Chem. Commun.*, 2011, **47**, 3436.
- 42 X. Li, A. Dhanabalan and C. Wang, *J. Power Sources*, 2011, **196**, 9625.
- 43 X. Li, A. Dhanabalan, K. Bechtold and C. Wang, *Electrochem. Commun.*, 2010, **12**, 1222.
- 44 Y. Fu, Z. Yang, X. Li, X. Wang, D. Liu, D. Hu, L. Qiao and D. He, *J. Mater. Chem. A*, 2013, **1**, 10002.
- 45 J. Jiang, Y. Y. Li, J. P. Liu, X. T. Huang, C. Z. Yuan and X. W. Lou, *Adv. Mater.*, 2012, **24**, 5166.
- 46 J. P. Liu, J. Jiang, C. W. Cheng, H. X. Li, J. X. Zhang, H. Gong and H. J. Fan, *Adv. Mater.*, 2011, **23**, 2076.
- 47 B. Liu, X. Wang, B. Liu, Q. Wang, D. Tan, W. Song, X. Hou, D. Chen and G. Shen, *Nano Res.*, 2013, **6**, 525–534.
- 48 M. V. Reddy, K. Y. H. Kenrick, Y. W. Tang, G. Y. Chong, G. H. Leong and B. V. R. Chowdari, *J. Electrochem. Soc.*, 2011, **158**, 1423–1430.
- 49 P. Balaya, H. Li, L. Kienle and J. Maier, *Adv. Funct. Mater.*, 2003, **13**, 621–625.
- 50 H. Li, X. J. Huang and L. Q. Chen, *Electrochem. Solid-State Lett.*, 1998, **1**, 241–243.
- 51 X. Wang, X. Li, X. Sun, F. Li, Q. Liu, Q. Wang and D. He, *J. Mater. Chem.*, 2011, **21**, 3571–3573.
- 52 S. Laruelle, S. Grugeon, P. Poizot, M. Dollé, L. Dupont and J. M. Tarascon, *J. Electrochem. Soc.*, 2002, **149**, A627.
- 53 G. Zhou, D. W. Wang, F. Li, L. Zhang, N. Li, Z. S. Wu, L. Wen, G. Q. Lu and H. M. Cheng, *Chem. Mater.*, 2010, **22**, 5306–5313.
- 54 M. S. Whittingham, *Dalton Trans.*, 2008, **37**, 5424.
- 55 Y. Wang, H. Zhang, L. Lu, L. P. Stubbs, C. Wong and J. Lin, *ACS Nano*, 2010, **4**, 4753–4761.
- 56 G. Q. Zhang, H. B. Wu, H. E. Hoster, M. B. Chan-Park and X. W. Lou, *Energy Environ. Sci.*, 2012, **5**, 9453.
- 57 Y. Wang, H. Li and Y. Xia, *Adv. Mater.*, 2006, **18**, 2619–2623.
- 58 G. Zhang and X. W. Lou, *Adv. Mater.*, 2013, **25**, 976–979.
- 59 C. Yuan, X. Zhang, L. Hou, L. Shen, D. Li, F. Zhang, C. Fan and J. Li, *J. Mater. Chem.*, 2010, **20**, 10809–10816.